COMMUNICATION

Check for updates

3D manipulation of cell spheroids using laser-actuated microrobots

Y. Wang, [ID] [abc] P. Harder, [abc] N. İyisan [abc] and B. Özkale [ID] *[abc]

Three-dimensional (3D) cell spheroids provide a powerful model for studying cellular behavior, tissue engineering, and drug screening. However, constructing heterogeneous microtissues from basic spheroids remains challenging, as it requires precise and biocompatible manipulation. Here, we present a method for 3D spheroid manipulation by incorporating microrobots, which, upon laser stimulation, induce thermophoretic fluid flow to actuate spheroid motion. The microrobots are incorporated into spheroids in a reliable manner, relying on cell-driven self-assembly. Locomotion of the microrobot-integrated spheroids is achieved by regulating the laser power (11.7–17.6 mW) and frequency (0.33 Hz), which leads to three characteristic modes of motion: jumping, vectoring, and pulling. The combination of these motions enables robust spheroid assembly with excellent biocompatibility. The system allows for the generation of complex tissue models, where fibrosarcoma (HT1080 cells) spheroids and healthy fibroblast (HDF cells) spheroids are assembled separately and then brought together using the microrobotic locomotion capabilities. The fusion of assembled HT1080 and HDF spheroids reveals cancer-stromal cell interactions and tissue integration, while a cancer-spheroid-centered radial arrangement of fibroblast spheroids demonstrates the construction of spatially sophisticated assembloids. This study establishes a versatile strategy for spheroid manipulation, advancing 3D microtissue biofabrication for *in vitro* disease modeling.

1. Introduction

Three-dimensional (3D) spheroid-based cell culture systems provide an essential set of tools for tissue engineering,[1–3] disease modeling,[4–6] and drug screening.[7–9] In contrast to conventional

[a] Microrobotic Bioengineering Lab (MRBL), School of Computation Information and Technology, Technical University of Munich, Hans-Piloty-Straße 1, 85748, Garching, Germany. E-mail: berna.oezkale@tum.de

[b] Munich Institute of Robotics and Machine Intelligence, Technical University of Munich, Georg-Brauchle-Ring 60, 80992, Munich, Germany

[c] Munich Institute of Biomedical Engineering, Technical University of Munich, Boltzmannstraße 11, 85748, Garching, Germany

New concepts

Constructing 3D physiological models *in vitro* requires precise positioning of cellular structures, such as spheroids. However, current manipulation methods are limited in selectivity, cell compatibility, and spatial precision. Here, we introduce photothermally responsive microrobots incorporated within spheroids, which generate thermo-convective flows to actuate controlled spheroid motion under laser actuation. This approach enables selective manipulation of individual spheroids, preserves cell viability, and achieves high-precision assembly of complex assembloid structures, providing a powerful new approach for biofabrication and tissue engineering.

two-dimensional (2D) cultures, 3D models more accurately recreate the physiological microenvironment by recapitulating cell–cell and cell-extracellular matrix (ECM) interactions, as well as gradients of nutrients, oxygen, and therapeutic agents.[10,11] Nevertheless, the construction of complex multi-spheroid structures (assembloids) is required to more accurately capture the complexity of tissue physiology and to fully investigate the dynamic 3D interactions among different cell lineages, which entails precise manipulation and spatial organization of spheroids.[12–14]

A variety of techniques have been developed to manipulate spheroids for the construction of organized 3D cellular structures. One of the earliest approaches was magnetic-assisted manipulation, in which spheroids composed of magnetically labelled cells were patterned using an external magnetic field.[15,16] This strategy requires labelling cells with magnetic materials, which can potentially impact cell function and cause cytotoxicity.[17] As a label-free alternative, acoustofluidic techniques employ standing acoustic waves to efficiently trap and position spheroids.[18] However, such field-driven approaches only offer global control over spheroid positioning, limiting the selectivity of spheroids for complicated microtissue assembly. To address this limitation, a microneedle-based system capable of generating localized acoustic fields was developed for the selective manipulation of individual spheroids.[19] This approach, however, carries the drawback that the direct contact between

the spheroid and the rapidly vibrating microneedle may impair cell function. Meanwhile, other strategies, including micro-pipette aspiration,[20] dielectrophoresis,[21] and photovoltaic tweezers,[22] have also been reported, yet these methods often expose cells to high mechanical stress or intense electrical fields, raising significant concerns about biocompatibility. There remains a need for contact-free and biocompatible methods that enable the precise manipulation of single spheroids with high selectivity and flexibility.

Light-driven microrobots and micromanipulators have emerged as promising candidates for contactless and high-precision micro-object manipulation.[23] However, conventional light-driven microrobots typically rely on chemical propulsion mechanisms, which can induce cytotoxic effects due to chemical stress.[24,25] More recently, laser-driven microrobots based on thermophoretic motion have been developed,[26–28] offering contact-free and selective microscale manipulation while main-taining cell compatibility through controllable and localized heating.

Here, we present a laser-driven microrobot-based approach for 3D manipulation of cell spheroids, enabling selective, biocompatible control *via* thermophoretic convection. Building on our previous work, we leveraged the thermally activated cell-signal imaging (TACSI)[26] microrobots to manipulate spheroids in 3D workspaces. We modify the design of TACSI microrobots by introducing RGD peptides to confer cell-adhesive properties and enable the self-assembly into cell–microrobot mixed spher-oids. Meanwhile, alginate hydrogels provide a biocompatible matrix for cell culture, gold nanorods (AuNRs) act as a laser-responsive heat source *via* surface plasmon resonance, and Rhodamine B (RhB) serves as a fluorescence-based temperature sensor, collectively enabling controlled locomotion through laser-induced thermophoretic fluid flow. The incorporated microrobots endow the spheroids with the ability to generate localized thermo-convection on a millimeter scale upon laser illumination, facilitating controlled multimodal spheroid loco-motion. As a proof of concept, the spheroid motion control technique is applied to assemble fibrosarcoma spheroids and fibroblast spheroids for fusion experiments, which confirms the cell viability and functionality with incorporated micro-bots after laser actuation. Furthermore, we constructed a radial structure consisting of a central cancer spheroid surrounded by multiple fibroblast spheroids to demonstrate the spatial preci-sion and flexibility of this spheroid manipulation method, which revealed its potential for high precision biofabrication of complex, multi-component assembloids and microtissues.

2. Results and discussion

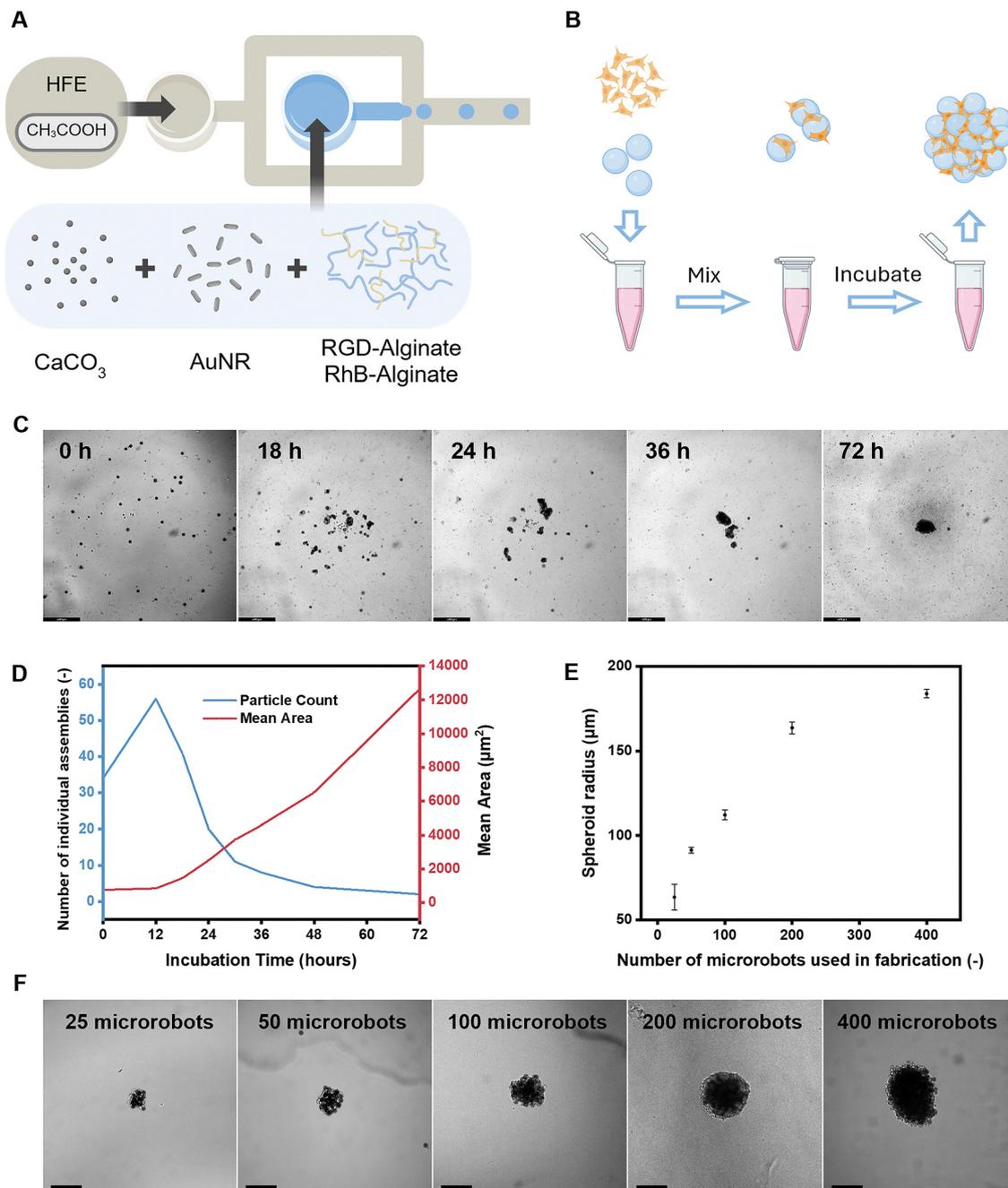### 2.1. Fabrication of microrobots and cell–microrobot spheroids

The TACSI microrobots were engineered from functional alginate components: RGD-alginate to promote cell adhesion,[29] RhB-alginate to enable temperature sensing,[30] and embedded AuNRs to provide photothermal actuation.[31] To fabricate these microrobots, we used a dual-phase cross-junction to produce aqueous droplets in an oil phase following our previously established protocol.[26,32] In this configuration, hydrofluoro-ether (HFE) containing acetic acid was injected into the oil-phase channel, where it intersected with the aqueous phase composed of 20% RhB-modified alginate and 80% RGD-modified alginate uniformly mixed with calcium carbonate ($CaCO_3$) nanoparticles and AuNRs (Fig. 1A). After droplet formation at the junction, acetic acid dissolved the $CaCO_3$ nanoparticles, releasing calcium ions that crosslinked the alginate polymers[33] to form structurally homogeneous microrobots.

The microrobots were systematically characterized to con-firm their morphology, size distribution, and the properties of the embedded gold nanorods. Bright-field optical microscopy (Fig. S1A and B, SI) revealed microrobots with well-defined, uniform spherical morphology and an average radius of 17.7 ± 1.1 μm (Fig. S2, SI). Scanning electron microscopy (SEM) of freeze-dried microrobots showed the overall microgel structure, and focused ion beam SEM (FIB-SEM) revealed a cross-section of the alginate scaffold containing sparsely and homogeneously distributed AuNRs, with only rare agglomerations (Fig. S1C and D, SI). The zeta potential of free AuNRs was measured to confirm their suitability for stable encapsulation within alginate *via* electrostatic interactions (Fig. S3, SI). Transmission electron microscopy (TEM) further confirmed the nanorod morphology with alginate encapsulation (Fig. S4, SI), and quantitative image analysis indicated an average size of 84.4 ± 7.4 nm × 23.4 ± 3.2 nm, consistent with previous reports.[26] Furthermore, UV-Vis spectroscopy (Fig. S5, SI) verified successful integration of AuNRs into the microrobots without compromising their photo-thermal properties, as indicated by retention of the character-istic absorbance peak with only a slight blue shift relative to free AuNRs, consistent with previous reports of AuNRs embedding in alginate matrices.[34,35]

To enable stable incorporation of microrobots into spher-oids, RGD peptides were introduced to promote integrin-mediated cell–material interactions. Rather than relying on passive aggregation, the assembly process is driven by active cell adhesion and cytoskeletal coupling, which facilitates the incorporation of microrobots during spheroid formation. The essential role of RGD decoration in spheroid formation was experimentally confirmed (Fig. S6, SI). This mechanism is con-sistent with previous studies showing that RGD-functionalized microstructures can be efficiently integrated into multicellular spheroids through integrin-dependent interactions.[36] Accord-ingly, the RGD-modified microrobots were mixed with cells at a defined microrobot-to-cell ratio (1:5) in low-adhesion, cone-shaped Eppendorf tubes, and after at least 48 hours of incuba-tion under cell culture conditions, they consistently self-assembled into spheroids as projected (Fig. 1B). To form single spheroids with controlled size and morphology, a one-spheroid-per-tube workflow was developed by limiting the number of microrobots (≤400) and cells (≤2000). Based on this workflow, the spheroid-forming process was then adapted to a U-shaped 96-well plate to enable time-lapse imaging. For this purpose, the wells were pre-coated with a thin layer of PDMS to minimize cell

Fig. 1 Fabrication and characterization of microrobot–cell spheroids. (A) Schematic of the microfluidic process used to fabricate microrobots. (B) Workflow for fabricating microrobot–cell spheroids by self-assembly: cells and microrobots are mixed in an Eppendorf tube and incubated for aggregation. (C) Time-lapse sequence of spheroid formation by self-assembly. Scale bar: 500 μm (D) Quantitative analysis of the assembly process, showing temporal changes in particle number within the field of view (blue) and the mean area of particle clusters (red). (E) and (F) Representative spheroid morphologies and corresponding equivalent radii generated using different initial microrobot numbers: (1) 25, (2) 50, (3) 100, (4) 200, and (5) 400. The cell-to-microrobot ratio was fixed at 5 : 1 across all conditions. Scale bar: 200 μm.

attachment. Initially, the cells and microrobots were randomly dispersed; however, over time, they gradually aggregated toward the central region of the U-shaped wells, where multiple microrobot–cell assemblies formed. After 72 h of incubation, these assemblies merged into a single 3D microrobot–cell structure (Fig. 1C). The self-assembly process was characterized by the counts and the average size of individual microrobot–cell assemblies (Fig. 1D). During the first 12 hours, the increasing number of assemblies indicated gravity-assisted gathering from outside the field of view into the center of the U-shaped well. Between 12 and 24 hours, the rapid decrease suggested extensive binding of single cells and microrobots into larger assemblies. Subsequently, once the major sub-assemblies had formed, the particle count gradually decreased to one, indicating integration

into the final structure. Moreover, the mean area of individual assemblies increased consistently over time, indicating progressive growth of the microrobot–cell structures. This trend suggests that cells actively pulled neighboring assemblies together, leading to the formation of larger integrated structures with homogeneously distributed microrobots (Fig. S7, SI).

We then investigated the fabrication of size-controlled single spheroids by modulating the number of microrobots and cells employed during the assembly process. Here, we varied the microrobot count from 25 to 400 while maintaining a constant microrobot-to-cell ratio of 1 : 5 (Fig. 1E). After 24 h of incubation, images of the spheroids were acquired (Fig. 1F), and their equivalent radii were calculated from the measured overviewed areas. Notably, spheroid size increased with the amount of initial assembly material; however, when 400 microrobots were employed, the increase was only marginal. This was because the excess microrobots and cells failed to fully merge into one single structure. Instead, they formed multiple microrobot–cell subassemblies. Conversely, when only 25 microrobots and 125 cells were used, the resulting spheroids exhibited a large deviation in size. This result was primarily due to the low concentration of the microrobots and cells, which reduced the likelihood of adhesive microrobots interacting with cells in suspension, leaving residual unbound units. In general, the optimal size-controlled spheroids were obtained with an intermediate microrobot count from 50 to 200 and corresponding cell numbers from 250 to 1000.

2.2. Laser-driven spheroid manipulation

We first investigated the photothermal performance of individual microrobots and spheroids to validate the laser actuation mechanism. To this end, the local temperature generated by laser actuation was quantified using RhB-based fluorescence thermometry. Calibration measurements on RhB-functionalized microrobots revealed a linear relationship between laser power and microrobot temperature, with the maximum power used for spheroid manipulation (17.6 mW) corresponding to an induced temperature of approximately 44 °C (Fig. S8, SI). The uniformity of photothermal response among the microrobots was validated through repeated experiments (Fig. S9, SI). In addition, temperature mapping of the surrounding medium confirmed that the laser-induced heating was highly localized around the illuminated spheroid and decayed rapidly with distance from the spheroid (Fig. S10, SI).

Next, we experimentally confirmed the thermal convection generated by the laser-actuated microrobot–cell spheroid through flow-field visualization using fluorescent tracer particles and quantified the corresponding velocity fields (Fig. S11–S13 and Movie S1, SI). With the microrobot–cell spheroid fixed at the bottom of the well plate under 785 nm laser illumination, the measured flow field demonstrated a circulating convective flow, characterized by upward flow near the spheroid and inward-directed flow toward the spheroid within the horizontal plane. In contrast, the pure cell spheroid did not generate any observable convection (Movie S2, SI). These observations validate that microrobot-mediated photothermal heating induces

convection, which may serve as the driving mechanism underlying spheroid motion.

After validating the generation of laser-induced circulating thermal convection, we investigated the resulting locomotion patterns of the microrobot–cell spheroids. Here, the fabricated spheroids were transferred into 96-well plates with wells coated by a thin layer of PDMS to reduce cell attachment to the well bottom. By adjusting the laser power and actuation frequency, three distinct thermo-convective flow fields were generated around the spheroid, enabling three motion modalities: jumping, vectoring, and pulling (Fig. 2A–C and Movie S3, SI).

The jumping motion is achieved by continuous high-power laser illumination on the microrobot-incorporated spheroid. As shown in Fig. 2A, the intense laser-induced heating generates a vigorous upward thermo-convective flow that produces a lifting force sufficient to overcome gravity as well as plate adhesion, thereby lifting the spheroid vertically out of the focal plane (Fig. 2D(1)–(3) and E(1)–(3)).

When the laser power is reduced below the threshold for jumping, the vertical lifting component of the thermo-convective flow becomes insufficient to elevate the spheroid, and the resulting motion transitions to predominantly horizontal displacement, termed vectoring (Fig. 2B). Here, we define vectoring as a reproducible unidirectional displacement of an actuated spheroid arising from asymmetry in the surrounding thermo-convective flow in the confined well geometry. When a spheroid is positioned away from the exact center of the well plate, laser-induced thermo-convection generates a net flow that pushes the spheroid radially outward from the well center. Due to the semi-symmetric confinement, this net flow is restricted to the radial axis, resulting in linear spheroid motion (Fig. 2D(3)–(4) and E(3)–(4)). To clarify the mechanism underlying vectoring, we examined the influence of spheroid position relative to the well boundary by analyzing flow fields using tracer particles. As shown in Fig. S11, the spheroid positioned off-center generated an asymmetric flow field, with relatively lower flow velocity on the side closer to the boundary. This boundary-influenced asymmetry became increasingly evident as the spheroid approaches the well wall, but diminished near the well center where confinement effects were minimal (Fig. S12 and Movie S4, SI). Consistently, in a larger 6-well plate, where boundary influence was reduced, both the overall flow magnitude and the flow asymmetry were substantially weaker (Fig. S13, SI). Moreover, asymmetric heating within the spheroid itself was ruled out as the origin of vectoring: regardless of the illumination position on the spheroid, laser actuation of the microrobots consistently produced the same vectoring direction (Movie S5, SI). These observations confirm that the unidirectional, boundary-seeking characteristic of vectoring in confined spaces is caused by the asymmetrical global thermal convection.

Beyond the vertical and horizontal single-spheroid motions, a multi-spheroid manipulation mode (pulling) can be achieved, in which one stationary target spheroid attracts one or more passive spheroids (Fig. 2C). In this mode, the target spheroid is continuously heated with a reduced power, generating a circulating convective flow weaker than that in the jumping motion.
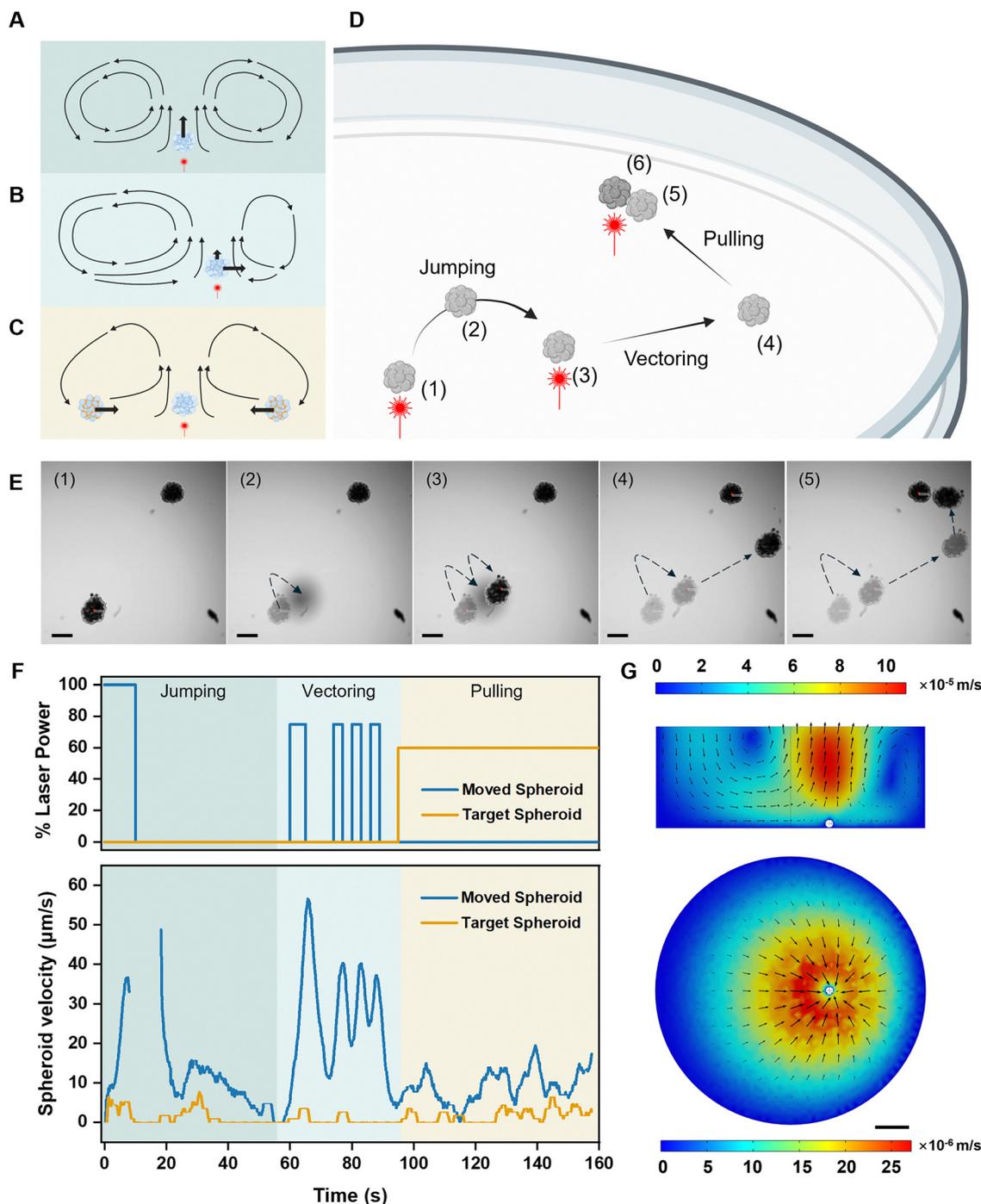
Fig. 2 Laser-actuated spheroid locomotion. (A)–(C) Schematic illustrations of spheroid manipulation modalities: (A) jumping, (B) vectoring, and (C) pulling. (D) Schematic showing a combined sequence of (1)–(3) jumping, (3)–(4) vectoring, and (4)–(5) pulling for the spatial assembly of two spheroids; the dark spheroid (6) denotes the stationary target. (E) Time-sequenced images of experimental spheroid manipulation toward the target following the same sequence of motions: (1)–(3) jumping, (3)–(4) vectoring, and (4)–(5) pulling. Scale bar: 200 μm. (F) Laser stimulation profile on the moved spheroid (blue) and the stationary target spheroid (orange), and corresponding spheroid horizontal speed during the three motion phases. (G) Numerical simulation of circulating thermal convection in a 96-well plate, presented in front and top views. Scale bar: 1 mm.

This circulating thermo-convection exerts a pulling effect on nearby passive spheroids, guiding them toward the target spheroid without lifting it. In the end, this interaction brings the passive spheroids into direct contact with the target spheroid (Fig. 2D(4)–(5) and E(4)–(5)). To evaluate the operational range of the pulling mode, we performed experiments with spheroids initially separated by distances of 442, 642, 1750, and 2370 μm. As shown in Fig. S14 and Movie S6 (SI), all separated spheroids were successfully brought into contact. For the largest separation distance, where the spheroids were positioned on

opposite sides of the well plate, alternating actuation of both spheroids enabled sustained thermophoretic motion and prevented prolonged adhesion to the well bottom. These results demonstrate that the pulling mode is effective over a wide range of initial distances. Notably, pulling provides a complementary capability to vectoring by enabling motion toward a target spheroid regardless of the boundary-seeking tendency of vectoring, thereby allowing spheroids to be guided back toward the central region of the well during manipulation.

Combining the above-mentioned motion mechanisms, we demonstrated the assembly of two spheroids in a 96-well plate (Fig. 2E and Movie S3, SI). To characterize the spheroid motion dynamics, a centroid-tracking program was used to measure the velocities of the spheroids (Movie S7, SI), and the corresponding velocity and laser actuation profiles are shown in Fig. 2F. Under the laser power of 17.6 mW, the spheroid rapidly ascended out of the focal plane while simultaneously vectoring toward the well boundary. When the laser was switched off, the spheroid gradually settled onto the well bottom, completing a 'forward jump' through the combined effects of lifting and vectoring. This jumping mode offers a practical strategy for 3D obstacle crossing, facilitating 3D spatial arrangement of spheroids for tissue engineering applications. At 60 s, a short-term on–off 14.5 mW laser stimulation induced vectoring-dominant motion. Despite reduced energy input, the spheroid exhibited rapid horizontal displacement, showing vectoring as an efficient and biocompatible 2D manipulation method. At 95 s, pulling was initiated by heating the stationary spheroid at a laser power of 11.7 mW, which gradually drove the moving spheroid into contact *via* thermo-convection. Notably, the stationary spheroid itself remained immobile (Fig. 2E and F), as the relatively low-power heating and thermo-convective drag from the moving spheroid were insufficient to overcome its adhesion to the plate. Thus, only specifically activated spheroids participated in the thermofluidic manipulation, ensuring high selectivity.

To support the interpretation of spheroid motion mechanisms, we further conducted numerical simulations to validate the convection patterns and quantify the stresses acting on the spheroid (Fig. 2G). Here, we modeled a 200-μm spheroid incorporating a 30-μm microrobot placed in a water domain in the geometry of a 96-well plate, 15 μm above the bottom. Heating the microrobot to 50 °C, a value consistent with experimentally measured laser-induced temperatures (Fig. S8, SI), generated a circulating thermo-convective flow (Fig. 2G). Front- and top-view slices through the spheroid center showed that the lifting flow reached velocities of up to 100 μm s^{-1}, whereas the center-directed pulling flow at a height of 30 μm reached up to 25 μm s^{-1}. These results are consistent with the experiments (Fig. 2F and Movie S3, SI), in which the jumping spheroid was rapidly lifted while the passive spheroid under pulling moved slowly. Moreover, the lifting and vectoring forces acting on the spheroid were calculated from a surface integral of the fluidic stress acting on the spheroid (Fig. S15, SI), further validating the dynamics of spheroid motion.

After investigating the controlled locomotion of jumping, vectoring, and pulling, we next assessed whether repeated laser actuation is compatible with living cells, as prolonged manipulation is required for building larger structures. For this purpose, spheroids comparable in size to those used for manipulation were exposed to continuous or periodic full-power laser heating (Fig. S16A and B, SI). There were no significant differences in cell viability among any of the actuated groups and the control group (Fig. S16C, SI). These viability results are consistent with the experimentally measured local temperature profiles (Fig. S8, SI), which indicate that cells experience only transient temperature around 44 °C. In summary, these experiments validated jumping, vectoring, and pulling as effective and selective spheroid manipulation modes, with viability assays confirming their biocompatibility under repeated laser actuation.

2.3. After manipulation: spheroid fusion characterization

After establishing the spheroid manipulation capabilities, we explored their post-assembly interactions as a proof-of-concept for applying this method to biological studies. Two types of spheroids, one composed of HT1080 cells and the other of human dermal fibroblasts (HDF), were introduced to investigate inter-spheroid interactions. Three spheroid pairs (HT1080–HT1080, HT1080–HDF, and HDF–HDF) were assembled using the laser-guided manipulation techniques described above. From Fig. 3A, we observed that the two attaching microrobot-incorporated spheroids gradually fused into one structure after 12–24 hours of incubation. This finding aligns with previous reports demonstrating fusion dynamics of cell-only spheroids within 24 hours.[37,38] To characterize the cell distribution during fusion, the two spheroids were stained with cell trackers of distinct fluorescent wavelengths. Particularly in the HT1080–HDF pair, HT1080 cells were labeled green and HDFs red. Based on these fluorescent cell trackers, we observed cell migration on the spheroid contact boundary. A small number of cells migrated into the foreign spheroid, exhibiting invasive behavior in the 3D microrobot–cell matrix. To quantify the degree of cell invasion, the average distance to the nearest foreign cell was defined as:

$$D_{A \to B} = \frac{1}{n_A} \sum_{i=1}^{n_A} \min_{1 \le j \le n_B} d(a_i, b_j) \qquad (1)$$

where $A = \{a_1, a_2, \ldots, a_{n_A}\}$ is the set of positions of type A cells; $B = \{b_1, b_2, \ldots, b_{n_B}\}$ is the set of positions of type B (foreign) cells; $d(x,y)$ is the distance between two cells. Smaller $D_{A \to B}$ values indicate deeper invasion of type B cells into the type A cluster. In practice, we adopted a pixel-sampling approach inspired by the Monte Carlo method to approximate the spatial distributions of red and green cells, as single cells are difficult to distinguish in 3D fluorescence images (Fig. 3B). As illustrated in Fig. 3C–E, the normalized distance to the nearest foreign cell in each spheroid decreased over time, indicating progressive intermixing of cells between the two original spheroids. We observed $D_{X \to HDF} < D_{Y \to HT}$ for X and Y of any cell type, particularly at the 24 h timepoint. This result suggests that
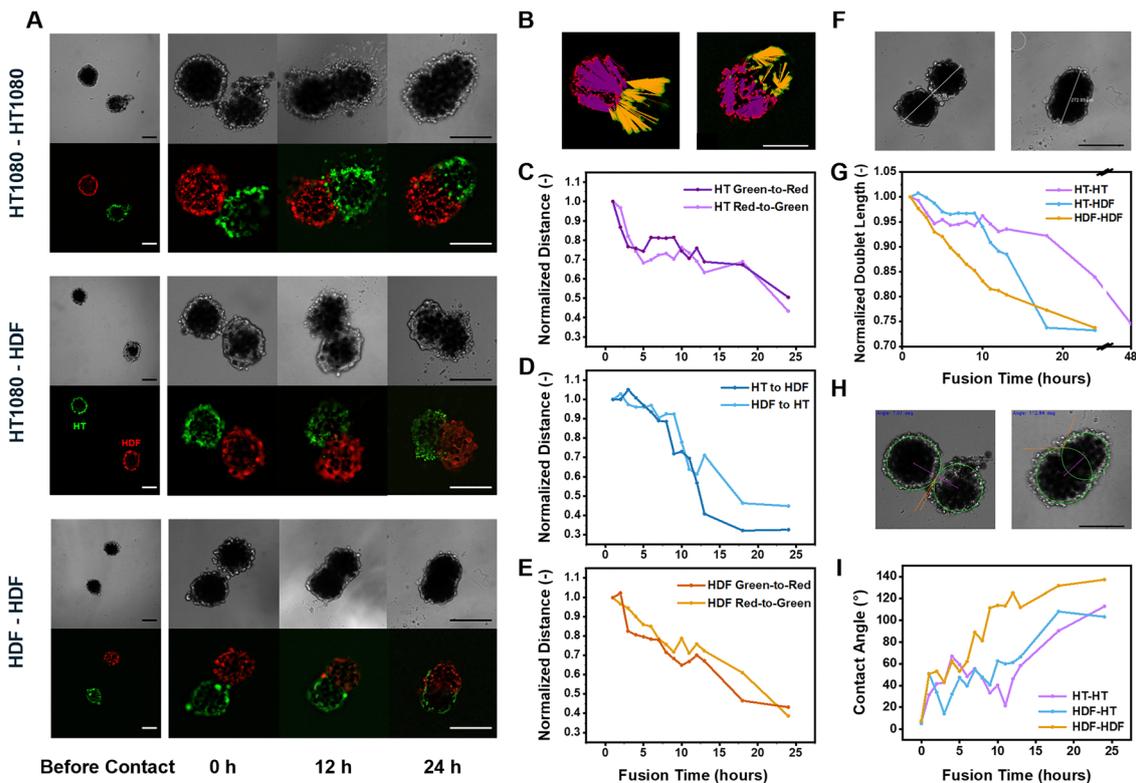
Fig. 3 Characterization of spheroid fusion dynamics. (A) Time-lapse images of the fusion process of fibrosarcoma (HT1080) spheroids and healthy human dermal fibroblast (HDF) spheroids in different pairings: HT1080−HT1080, HT1080−HDF, and HDF−HDF. In the HT1080−HDF group, HT1080 spheroids were labeled green and HDF spheroids red using cell trackers of different wavelengths. (B)−(I) Quantitative analysis of spheroid fusion is presented, including (B)−(E) average distance to the nearest foreign cells, (F) and (G) doublet length (distance between the farthest points of the dual-spheroid structure), and (H) and (I) contact angle. (B), (F) and (H) Representative images illustrate the measurement of morphological metrics. (C)−(E) Normalized distance to the nearest foreign cells in the three spheroid pairings is presented for three types of assembloids: (C) HT1080−HT1080, (D) HT1080−HDF, and (E) HDF−HDF. (G) Doublet length and (I) contact angle measurements are plotted over fusion time for HT1080−HT1080, HT1080−HDF, and HDF−HDF assembloids. Scale bars: 200 μm.

more HDFs than HT1080 cells migrated into the neighboring spheroid during the fusion process. This phenomenon is consistent with previous reports showing that cancer cells can biochemically activate fibroblasts into cancer-associated fibroblasts (CAFs), thereby promoting fibroblast proliferation and extracellular matrix remodeling,[39,40] which may facilitate fibroblast migration and settlement within neighboring spheroids.

On the spheroid scale, we characterized spheroid fusion rate by measuring the distance between the farthest points of the dual-spheroid structure (doublet length, Fig. 3F), which decreased over time, indicating enhanced tissue cohesion during fusion (Fig. 3G). Notably, the two HDF-involved fusion groups exhibited faster volume reduction than the HT-HT spheroids, which was consistent with the ECM contraction behavior of fibroblasts,[39,41] secreting ECM[42] to form a tight microtissue. We then measured the contact angle of the dual-spheroid structure as a morphological metric (Fig. 3H), where the rise in contact angle (Fig. 3I) reflected the rearrangement of cells and microrobots at the spheroid confrontation boundary, with cells migrating to fill the inter-spheroid gap. In accordance with these observations, the HDF−HDF spheroids showed the

fastest increase in contact angle compared to mixed and pure HT spheroids.

2.4. Spheroids as building blocks for complex tissue construction

The successful fusion of spheroids highlights their potential as building blocks for complex tissue construction. With our approach, spheroids can be heterogeneously assembled through microrobotic manipulation, thereby substantially increasing the spatial complexity of tissue structures. To demonstrate the feasibility and precision of this strategy, we constructed a radial arrangement of spheroids, placing a central HT1080 cancer spheroid surrounded by multiple healthy HDF spheroids (Fig. 4A and Movie S8, SI). Using a combination of pulling, vectoring, and 3D jumping motions, spheroids were assembled into defined spatial configurations, specifically, satellite spheroids surrounding a central core (Movie S8, SI). Interestingly, multi-spheroid constructs (assembloids) exhibited rotational motion under asymmetric laser actuation, which was not observed within single spheroids. This observation is likely due to the magnitude of torque derived by the higher thermo-convective flow in larger constructs.
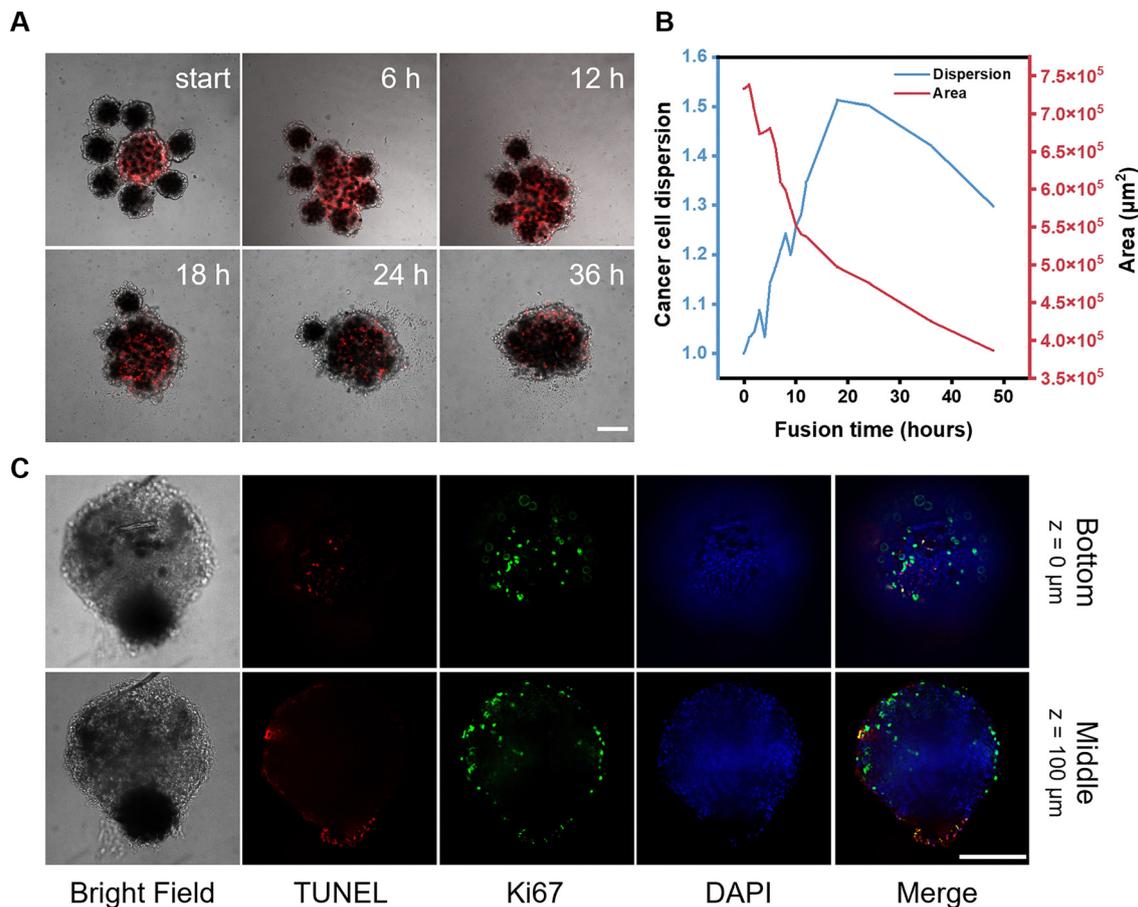
Fig. 4 Fusion of radial spheroid structure. (A) Time-lapse images showing spheroid fusion in a radial configuration. The red fluorescent dye-labeled spheroid represents an HT1080 cancer cell spheroid, surrounded by unlabeled fibroblast spheroids. Scale bar: 200 μm. (B) Quantitative analysis of the fusion process, depicting temporal changes in cancer cell dispersion (blue) and the overall structure area (red). Dispersion was calculated as the normalized mean distance of fluorescently labeled cells from their centroid. (C) TUNEL–Ki67 staining of the final three-dimensional structure after completion of the fusion process. Scale bar: 200 μm.

Cancer cells were labeled with cell tracking fluorescent probes to distinguish them from HDFs during tissue formation. In the first 24 h, six satellite spheroids in direct contact with the central cancer spheroid fused into a single assembloid, while the remaining HDF spheroid fused at 36 h. Notably, the top-left two HDF spheroids, which directly contacted both HDF and HT1080 spheroids, fused preferentially with the HT1080 spheroid. This observation might suggest the cancer-induced activation of fibroblasts into CAFs, enhancing their ability to form new cellular structures.[43] Meanwhile, cancer cells spread and dispersed widely within the fused 3D structure. The dispersion of cancer cells, quantified by their normalized mean distance from the geometric centroid, increased continuously during the first 18 h (Fig. 4B), suggesting migration. As reported by previous studies, ECM remodelling,[44] intercellular signalling,[45] and mechanical coupling[43] can facilitate cancer cell migration and invasion, which could provide a possible explanation for the observed dispersion of HT1080 cells. After 18 h, cell dispersion slightly decreased as a result of assembloid shrinkage (Fig. 4B), which was additionally quantified by measuring the total projected area of the structure.

To ensure the cell health was maintained in the fused assembloid, we investigated changes in apoptotic and proliferative behavior using a standard TUNEL assay along with Ki67 immunostaining. As shown in Fig. 4C, apoptotic and proliferating cells were observed in both the bottom and middle layers of the microtissue. The signals localized mainly at the boundary of the 3D assembloid, as a consequence of limited fluorescence imaging quality in the interior. Notably, in the middle layer, numerous apoptotic signals were detected in the latest fused spheroid (dark), suggesting a possible association between apoptosis and impeded spheroid fusion. In comparison with the control groups of pure HT1080 and HDF spheroids (Fig. S17, SI), the percentage of apoptotic cells in the assembloid was similar, suggesting that the spheroid manipulation and fusion process did not induce notable apoptosis. Furthermore, HT1080 cells in the control group exhibited a substantially higher proliferation rate, whereas HDFs rarely expressed Ki67, indicating that the majority of proliferating cells were cancer cells. Accordingly, the percentage of Ki67-positive cells in the assembloid was lower than in pure HT1080 spheroids but higher than in pure HDF spheroids. Overall, the

cancer-spheroid-centered radial arrangement of fibroblast spheroids highlighted the potential of thermo-convection-mediated manipulation for constructing complex assembloids and microtissues.

3. Conclusion

In summary, we demonstrate 3D manipulation of microrobot-incorporated cell spheroids through laser-induced thermo-convection. The self-assembly of cells with cell-adhesive micro-robots enables convenient and reproducible fabrication of single microrobot–cell spheroids. Under different laser stimulation profiles, spheroids exhibit three distinct motion modalities: jumping, vectoring, and pulling, which facilitated their assembly with spatial control. As a proof of concept, the fusion of assembled HT1080 and HDF spheroids demonstrates three-dimensional interactions between cancer cells and fibroblasts, highlighting the potential of this platform for biologically relevant applications. The exquisite radial arrangement of spheroids further illustrates the capability of the thermo-convection-mediated spheroid manipulation to form complex cancer–fibroblast assembloids with high precision and biocompatibility, revealing the potential of this approach for studying 3D cell behaviour and constructing microtissue.

This work lays the foundation for microrobot-assisted spheroid manipulation and provides a versatile toolset for the 3D construction of heterogeneous micro-organoids and tumor microenvironments. Building on this technique, we aim to construct sophisticated multicellular 3D assembloids that better mimic physiological conditions and extend the capabilities of *in vitro* physiological models for biological and pharmaceutical investigations. Furthermore, this platform opens opportunities for localized and spatiotemporally controlled stimulation within assembloids. By leveraging photothermal actuation and incorporating functional materials into the microrobots, future studies may enable controlled modulation of local temperature, mechanical stress, or chemical microenvironments within spheroids and organoids. Such localized stimulation strategies could facilitate systematic studies of cell migration, tissue remodeling, and intercellular signaling in three-dimensional microtissues, which remain challenging to achieve using conventional culture and assembly techniques.

Conflicts of interest

There are no conflicts to declare.

Data availability

The data supporting this article have been included as part of the supplementary information (SI). The SI contains the experimental section, supporting figures, and a list of supplementary videos related to this study. See DOI: https://doi.org/10.1039/d5mh01861g.

References

1 M. W. Laschke and M. D. Menger, *Trends Biotechnol.*, 2017, **35**, 133–144.

2 V. F. Fiore, J. Almagro and E. Fuchs, *Nat. Rev. Mol. Cell Biol.*, 2025, **26**, 442–455.

3 P. N. Nwokoye and O. J. Abilez, *Cells Rep. Methods*, 2024, **4**, 100779.

4 R. Polak, E. T. Zhang and C. J. Kuo, *Nat. Rev. Cancer*, 2024, **24**, 523–539.

5 H. Koike, K. Iwasawa, R. Ouchi, M. Maezawa, K. Giesbrecht, N. Saiki, A. Ferguson, M. Kimura, W. L. Thompson, J. M. Wells, A. M. Zorn and T. Takebe, *Nature*, 2019, **574**, 112–116.

6 H. T. Ong, E. Karatas, T. Poquillon, G. Grenci, A. Furlan, F. Dilasser, S. B. Mohamad Raffi, D. Blanc, E. Drimaracci, D. Mikec, G. Galisot, B. A. Johnson, A. Z. Liu, C. Thiel, O. Ullrich, A. Vincent, V. Racine, A. Beghin and R. E. S. C. Orga, *Nat. Methods*, 2025, **22**, 1343–1354.

7 J. Xie, Q. Yang, Y. Zhang, K. Zheng, H. Geng and Y. Wu, *Adv. Sci.*, 2025, **12**, 2416863.

8 D. Ascheid, M. Baumann, J. Pinnecker, M. Friedrich, D. Szi-Marton, C. Medved, M. Bundalo, V. Ortmann, A. Öztürk, R. Nandigama, K. Hemmen, S. Ergün, A. Zernecke, M. Hirth, K. G. Heinze and E. Henke, *Nat. Commun.*, 2024, **15**, 3599.

9 E. Driehuis, K. Kretzschmar and H. Clevers, *Nat. Protoc.*, 2020, **15**, 3380–3409.

10 J. C. Fontoura, C. Viezzer, F. G. dos Santos, R. A. Ligabue, R. Weinlich, R. D. Puga, D. Antonow, P. Severino and C. Bonorino, *Mater. Sci. Eng., C*, 2020, **107**, 110264.

11 G. Rauner, P. B. Gupta and C. Kuperwasser, *Nat. Methods*, 2025, **22**(9), 1776–1787.

12 N. Vogt, *Nat. Methods*, 2021, **18**, 27.

13 M. M. Onesto, J.-i Kim and S. P. Pasca, *Cell Stem Cell*, 2024, **31**, 1563–1573.

14 T. Zhu, Y. Hu, H. Cui and H. Cui, *Adv. Healthcare Mater.*, 2024, **13**, 2400957.

15 V. H. B. Ho, K. H. Müller, A. Barcza, R. Chen and N. K. H. Slater, *Biomaterials*, 2010, **31**, 3095–3102.

16 A. Tocchio, N. G. Durmus, K. Sridhar, V. Mani, B. Coskun, R. El Assal and U. Demirci, *Adv. Mater.*, 2018, **30**, 1705034.

17 E. Vuille-dit-Bille, D. V. Deshmukh, S. Connolly, S. Heub, S. Boder-Pasche, J. Dual, M. W. Tibbitt and G. Weder, *Lab Chip*, 2022, **22**, 4043–4066.

18 B. Chen, Z. Wu, Y. Wu, Y. Chen and L. Zheng, *Microfluid. Nanofluid.*, 2023, **27**, 50.

19 Q. Yin, K. Chen, C. Zhou, Y. Su, X. Yu, S. Feng, X. Wang, Z. Ma and W. Zhang, *Int. J. Extreme Manuf.*, 2025, **7**, 045501.

20 B. Ayan, D. N. Heo, Z. Zhang, M. Dey, A. Povilianskas, C. Drapaca and I. T. Ozbolat, *Sci. Adv.*, 2020, **6**, eaaw5111.

21 M. Schimpf, PhD thesis, Technische Universität Wien, 2023.

22 E. Rincón, P. Camarero, M. Quintanilla, A. Méndez, A. García-Cabañes, P. Haro-González and M. Carrascosa, *Adv. Photonics Res.*, 2024, 2400124.

23 S. Palagi, D. P. Singh and P. Fischer, *Adv. Opt. Mater.*, 2019, **7**, 1900370.

24 L. Xu, F. Mou, H. Gong, M. Luo and J. Guan, *Chem. Soc. Rev.*, 2017, **46**, 6905–6926.

25 R. Dong, Y. Cai, Y. Yang, W. Gao and B. Ren, *Acc. Chem. Res.*, 2018, **51**, 1940–1947.

26 P. Harder, N. İyisan, C. Wang, F. Kohler, I. Neb, H. Lahm, M. Dreßen, M. Krane, H. Dietz and B. Özkale, *Adv. Healthcare Mater.*, 2023, **12**, 2300904.

27 X. Wu, R. Ehehalt, G. Razinskas, T. Feichtner, J. Qin and B. Hecht, *Nat. Nanotechnol.*, 2022, **17**, 477–484.

28 Z. Guo, T. Liu, W. Gao, C. Iffelsberger, B. Kong and M. Pumera, *Adv. Mater.*, 2023, **35**, 2210994.

29 U. Hersel, C. Dahmen and H. Kessler, *Biomaterials*, 2003, **24**, 4385–4415.

30 D. Moreau, C. Lefort, R. Burke, P. Leveque and R. P. O'Connor, *Biomed. Opt. Express*, 2015, 4105–4117.

31 J. Cao, T. Sun and K. T. V. Grattan, *Sens. Actuators, B*, 2014, **195**, 332–351.

32 B. Özkale, J. Lou, E. Özelçi, A. Elosegui-Artola, C. M. Tringides, A. S. Mao, M. S. Sakar and D. J. Mooney, *Lab Chip*, 2022, **22**, 1962–1970.

33 S. Utech, R. Prodanovic, A. S. Mao, R. Ostafe, D. J. Mooney and D. A. Weitz, *Adv. Healthcare Mater.*, 2015, **4**, 1628–1633.

34 Y. L. Loke, A. Beishenaliev, P.-W. Wang, C.-Y. Lin, C.-Y. Chang, Y. Y. Foo, F. N. Faruqu, B. F. Leo, M. Misran, L. Y. Chung, D.-B. Shieh, L. V. Kiew, C.-C. Chang and Y. Y. Teo, *Ultrason. Sonochem.*, 2023, **96**, 106437.

35 M. Manimaran, Y. Y. Teo, J. C. Y. Kah, A. Beishenaliev, Y. L. Loke, Y. Y. Foo, S.-F. Ng, C. F. Chee, S. P. Chin and F. N. Faruqu, *Int. J. Nanomed.*, 2024, 3697–3714.

36 T. Kamperman, N. G. A. Willemen, C. Kelder, M. Koerselman, M. Becker, L. Lins, C. Johnbosco, M. Karperien and J. Leijten, *Adv. Sci.*, 2023, **10**, 2205487.

37 R. Pan, C. Lin, X. Yang, Y. Xie, L. Gao and L. Yu, *Biofabrication*, 2024, **16**, 035016.

38 N. V. Kosheleva, Y. M. Efremov, B. S. Shavkuta, I. M. Zurina, D. Zhang, Y. Zhang, N. V. Minaev, A. A. Gorkun, S. Wei, A. I. Shpichka, I. N. Saburina and P. S. Timashev, *Sci. Rep.*, 2020, **10**, 12614.

39 L. Moretti, J. Stalfort, T. H. Barker and D. Abebayehu, *J. Biol. Chem.*, 2022, **298**, 101530.

40 G. Biffi and D. A. Tuveson, *Physiol. Rev.*, 2020, **101**, 147–176.

41 P. Pakshir, M. Alizadehgiashi, B. Wong, N. M. Coelho, X. Chen, Z. Gong, V. B. Shenoy, C. A. McCulloch and B. Hinz, *Nat. Commun.*, 2019, **10**, 1850.

42 B. Hinz, *J. Biomech.*, 2010, **43**, 146–155.

43 Y. Chhabra and A. T. Weeraratna, *Cell*, 2023, **186**, 1580–1609.

44 A. Glentis, P. Oertle, P. Mariani, A. Chikina, F. El Marjou, Y. Attieh, F. Zaccarini, M. Lae, D. Loew, F. Dingli, P. Sirven, M. Schoumacher, B. G. Gurchenkov, M. Plodinec and D. M. Vignjevic, *Nat. Commun.*, 2017, **8**, 924.

45 B. Erdogan and D. J. Webb, *Biochem. Soc. Trans.*, 2017, **45**, 229–236.